



Tetragonal NaVPO₄F@rGO nanocomposite as a high-rate cathode for aqueous zinc-ion batteries†

 Cite this: *Chem. Commun.*, 2025, 61, 3339

 Received 28th November 2024,
 Accepted 24th January 2025

DOI: 10.1039/d4cc06315e

rsc.li/chemcomm

A tetragonal NaVPO₄F coated with reduced graphene oxide (rGO) manifests an outstanding high-rate capability of 90.6 mA h g⁻¹ at 10C and a stable capacity of 41.9 mA h g⁻¹ after 4000 cycles at 30C owing to the enhanced electronic conductivity and improved Zn²⁺ diffusion capability from the rGO coating.

While lithium-ion batteries are characterized by their elevated energy density and stability, their utilization in electric vehicles and portable devices has revealed considerable challenges, including safety issues, resource limitations, and increasing costs, which impede their broader application.¹ In comparison, zinc is identified as a more stable, affluent, and secure anode, its ionic radius of Zn²⁺ (0.74 Å) approximately aligning with that of Li⁺ (0.76 Å).^{2–5} Zinc anodes exhibit a low redox potential of –0.76 V relative to the standard hydrogen electrode (SHE) and a significant theoretical specific capacity of 820 mA h g⁻¹ or 5851 mA h cm⁻³.^{6–11} The use of aqueous electrolytes in zinc-ion batteries guarantees elevated ionic conductivity (~1.0 S cm⁻¹), enhanced safety, and cost-effectiveness, rendering them especially appropriate for extensive energy storage applications.³ Nonetheless, the interaction between divalent zinc ions and cathode materials hinders reaction kinetics and reduces cycling performance, thereby limiting the development of aqueous zinc-ion batteries (AZIBs).^{12,13} Recently, the polyanionic materials, such as vanadium phosphate cathodes, with large ion diffusion channels, excellent structural stability, and high voltage, have gained significant attention.¹⁴ Hu *et al.* reported that Na₃V₂(PO₄)₃/reduced graphene oxide (rGO) achieved a notable capacity of 114.0 mA h g⁻¹ and an average discharge plateau of 1.2 V at 0.05 A g⁻¹.¹⁵

Jiang's group discovered that Na₃V₂(PO₄)₂F₃@C, obtained by a sol-gel method, represented a high voltage plateau of 1.6 V and a reversible capacity of 62.0 mA h g⁻¹ at 0.2 A g⁻¹.¹⁶ The enhanced voltage platform is attributed to the introduction of F⁻ with high electronegativity. Notably, compared to Na₃V₂(PO₄)₃ (117 mA h g⁻¹) and Na₃V₂(PO₄)₂F₃ (128.0 mA h g⁻¹), NaVPO₄F (NVPF) delivers a larger theoretical capacity (143.0 mA h g⁻¹).¹⁷

In 2010, Zhao *et al.* successfully synthesized monoclinic NVPF with elevated rate properties and specific capacities exceeding 120 mA h g⁻¹ in sodium-ion batteries (SIBs).^{18,19} However, its low operating voltage (3.4 V) restricts further enhancement in energy density. Conversely, the tetragonal NVPF, initially reported by Barker in 2003, exhibited a relatively higher operating voltage of 3.8 V in SIBs.²⁰ In 2017, Chang *et al.* synthesized tetragonal NVPF through solvothermal synthesis, yielding a capacity of 80.0 mA h g⁻¹ at 1C in SIBs.²¹ This low capacity was ascribed to its large particle size and the absence of carbon coating. Despite the inadequate performance of unmodified NVPF, the implementation of a cooperative strategy involving graphene coating and a reduction in particle size enhanced its capacity to 120.9 mA h g⁻¹ at 0.05C. Due to the non-uniform electron transfer on the uneven carbon coating, the capacity at 0.5C dropped sharply to 70.1 mA h g⁻¹. In 2021, Xia *et al.* reported that the monoclinic NVPF was employed as a cathode material for AZIBs, produced by the sol-gel process.²² It achieved a capacity of 89.7 mA h g⁻¹ at 0.05 A g⁻¹, accompanied by a stable working voltage of 1.36 V, indicating its viability as a zinc storage cathode material.

NVPF exists two phases including a tetragonal phase, resembling Na₃Al₂(PO₄)₂F₃, and a monoclinic phase, analogous to NaAlPO₄F.²³ The two crystal structures consist of [V₂O₈F₃] and [PO₄] polyhedral units with distinct angular framework configurations that promote ion transport.²⁴ Nonetheless, their low electronic conductivity, attributed to a wide band gap (~2 eV), poses a performance limitation that can be mitigated by incorporating conductive composites, doping, and nano-engineering techniques.^{3,25} Notably, NVPF undergoes a phase transition from tetragonal to monoclinic with increasing temperature,

^a School of Materials and Energy, Guangdong University of Technology, Guangzhou 510006, Guangdong, China.

E-mail: shaolianyi@gdut.edu.cn, zpsunxj@gdut.edu.cn

^b Key Laboratory of Advanced Electrode Materials for Novel Solar Cells for Petroleum and Chemical Industry of China, School of Chemistry and Life Sciences, Suzhou University of Science and Technology, Suzhou 215009, Jiangsu, China. E-mail: juzi147@163.com

† Electronic supplementary information (ESI) available: Experimental section, supporting figures and tables. See DOI: <https://doi.org/10.1039/d4cc06315e>

highlighting the importance of obtaining tetragonal NVPF with superior performance through low-temperature calcination. However, challenges arise from uneven carbon coating at the low-temperature calcination, impacting electronic conductivity. Therefore, the advancement of NVPF applications lies in exploring methods to obtain tetragonal NVPF nanoparticles with a well-formed carbon coating at low temperature. Simultaneously, the zinc storage property of the tetragonal NVPF is an unexplored area.

In this work, a hydrothermal and post-calcination method has been proposed to encapsulate NVPF nano-rectangular blocks within rGO, resulting in the formation of three-dimensional composites designated as NVPF@rGO. This methodology effectively promotes the uniform distribution of NVPF particles, enhances the Zn^{2+} diffusion coefficient, and lowers resistance. Hence, as a cathode for AZIBs, the electrode exhibits exceptional electrochemical properties, offering a notable capacity of $143.1 \text{ mA h g}^{-1}$ at 1C (143.0 mA g^{-1}), outstanding rate performance of 64.4 mA h g^{-1} at 30C, and super cycling stability with a reversible capacity of 41.9 mA h g^{-1} after 4000 cycles at 30C.

Fig. 1a depicts the synthetic procedure of NVPF, using a hydrothermal technique followed by low-temperature calcination. Specifically, solution A was prepared by dissolving $\text{C}_{10}\text{H}_{14}\text{O}_5\text{V}$ in ethanol, while solution B was created by mixing NaF and $\text{NH}_4\text{H}_2\text{PO}_4$ in water. Upon mixing the two solutions, graphene oxide solution was then added to form solution C. Solution C was then placed in a polytetrafluoroethylene reactor, heated at 120°C for 2 hours, washed, and dried to obtain the precursor, which was then calcined at 450°C for 8 hours to yield NVPF@rGO. As illustrated in Fig. 1b, the material maintains a single tetragonal phase after rGO coating at low temperatures ranging from 250 to 450°C (NVPF@rGO-1, NVPF@rGO-2, and NVPF@rGO-3). As the calcination temperature increases, the diffraction peak intensity of NVPF@rGO gradually strengthens, demonstrating enhanced crystallization

of NVPF@rGO at higher temperatures. Increasing the calcination temperature to 550°C (NVPF@rGO-4), numerous hybrid peaks appear at 10° – 35° , indicating the inability to form tetragonal NVPF at 550°C . Rietveld's refinement reveals that all diffraction peaks can be indexed to the tetragonal NaVPO_4F shown in Fig. 1c and Table S1 (ESI[†]), whose structure is similar to that of $\text{Na}_3\text{Al}_2(\text{PO}_4)_2\text{F}_3$ with a space group of $I4/mmm$.^{20,23} The principal peaks are situated at 16.1° , 16.5° , 27.9° , 28.5° , and 32.6° , corresponding to the (101), (002), (200), (103), and (202) crystal faces. The Na sites are distributed within the three-dimensional channels made by the $[\text{PO}_4]$ tetrahedron and $[\text{VO}_2\text{F}_4]$ octahedron through sharing O atoms, as depicted in Fig. 1a. While their corners are shared, the $-\text{O}-\text{V}-\text{O}-\text{P}-\text{O}-$ chain is eventually generated, providing a fast Na^+ transport path in the crystal structure.^{24,26}

Two characteristic peaks observed at 1342 and 1587 cm^{-1} correspond to the D band (disordered carbon) and the G band (graphitized carbon) for rGO, respectively.²⁷ The intensity ratio of the D band to the G band ($I_{\text{D}}/I_{\text{G}}$) for NVPF@rGO-1, NVPF@rGO-2, and NVPF@rGO-3 is 1.12, 1.13, and 1.15, respectively, as shown in Fig. 1d and Fig. S1 (ESI[†]), suggesting that the carbon in NVPF@rGO is predominantly in an amorphous state with much defects, thereby improving its electrochemical activity. Additionally, with the increase of calcination temperature, the $I_{\text{D}}/I_{\text{G}}$ value also rises, indicating that higher temperature facilitates the formation of amorphous carbon. This phenomenon leads to an increase in defects, consequently enhancing the electrochemical performance.

X-ray photoelectron spectroscopy (XPS) was also used to analyze the chemical composition and valence states of the NVPF@rGO-3 composites. The survey spectrum in Fig. S2 (ESI[†]) shows the presence of Na, V, P, O, F, and C elements in NVPF@rGO-3. In the C 1s spectrum, three peaks at 284.8, 285.7, and 288.4 eV correspond to the C=C, C-O-C, and O-C=O bonds, respectively, derived from rGO in Fig. 1e.²⁸ The intensity of the O-C=O bond is much weaker than that of the C=C bond due to the carbothermal reaction during the calcination process for the generation of rGO. In addition to the C-O-C and O-C=O functional groups, the carbon atoms predominantly exhibit the sp^2 hybridization, which implies that NVPF@rGO is enveloped by electron clouds originating from the conjugated 2p orbitals, enhancing the electronic conductivity.²⁸ The V 2p spectrum displays V 2p_{1/2} and V 2p_{3/2} peaks at 517.5 and 525.0 eV in Fig. 1f, attributed to V^{3+} in NVPF@rGO.²¹ Three peaks at 530.8, 531.7, and 532.6 eV in Fig. 1g can be assigned to the P-O, C-O, and V-O bands.²³ Compared to pure NVPF (Fig. S3, ESI[†]), these peaks are basically unchanged after coating rGO, further demonstrating that the incorporation of rGO in the synthetic process cannot influence the ultimate structure and element valence of NVPF.

Scanning electron microscopy (SEM) and transmission electron microscopy (TEM) were used to characterize the morphological and structural features of the acquired samples. The variations in particle sizes for NVPF and NVPF@rGO-1/2/3 can be detected in Fig. 2a, b and Fig. S4 (ESI[†]). In the presence of rGO, the particles evolve into more uniform nano-rectangular



Fig. 1 (a) Production process and crystal structure of NVPF. (b) XRD patterns of NVPF@rGO at different temperatures. (c) Rietveld's refinement of NVPF@rGO-3. (d) Raman curves of NVPF@rGO-3 and NVPF. XPS spectra of (e) C 1s, (f) V 2p, and (g) O 1s.

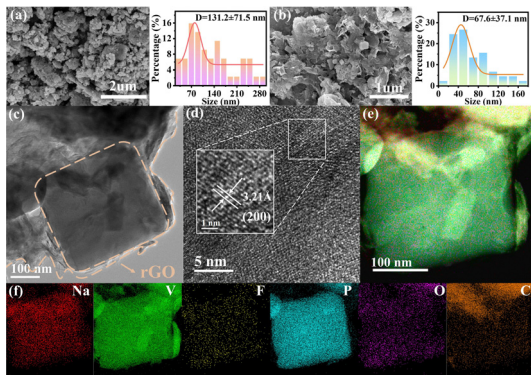


Fig. 2 SEM images and particle sizes of (a) NVPF and (b) NVPF@rGO-3. (c) TEM, (d) HRTEM, and (e) and (f) TEM EDS mapping images of NVPF@rGO-3.

blocks at higher temperatures compared to pure NVPF. Besides, the particle sizes decrease as the calcination temperature rises. These phenomena suggest that the morphology and dimensions of NVPF can be controlled by incorporating the addition of rGO and the increased calcination temperature. The NVPF nano-rectangular blocks in NVPF@rGO-3 are also verified through the TEM image presented in Fig. 2c, where the rGO carbon layer is intimately attached to the surface of the NVPF particles, thereby stabilizing the structure of NVPF@rGO and improving its electrical conductivity. Besides, the interplanar spacing of 0.32 nm is observed in Fig. 2d, linking to the (200) crystal plane of NVPF. Fig. 2e and f further demonstrate a homogeneous distribution of Na, V, P, O, F, and C on the surface of the NVPF particles.

Cyclic voltammetry (CV) and galvanostatic charge–discharge techniques were utilized to assess the electrochemical characteristics of NVPF and NVPF@rGO-3. Fig. 3a illustrates the CV curves of NVPF and NVPF@rGO-3. The oxidation peaks at 1.02, 1.28, 1.55, and 1.78 V are due to the detachment of Na^+ from the NVPF. The associated reduction peaks at 0.87, 1.18, 1.35, and 1.66 V correspond to the entrance of Zn^{2+} into NVPF.²³ The curve area for NVPF@rGO-3 is larger than that for NVPF, indicating the improved performance after rGO coating. The initial discharge and charge profiles of NVPF and NVPF@rGO-3 at 1C (143.0 mA g^{-1}) are presented in Fig. S5 (ESI[†]). NVPF@rGO-3 demonstrates a

discharge capacity of 129.7 mA h g^{-1} , surpassing that of NVPF (110.7 mA h g^{-1}). Unlike sodium ion batteries, the less distinct discharge plateaus of NVPF@rGO in AZIBs are ascribed to the considerable resistance that must be overcome when Zn^{2+} enters into the NVPF structure, as a result of the strong electrostatic force exerted by Zn^{2+} .²⁹ After 10 cycles, the battery system stabilizes with a Coulombic efficiency of 99%. In Fig. 3b, the capacity of NVPF@rGO-3 is 143.1 mA h g^{-1} after 50 cycles, closely aligning with the theoretical capacity of 143.0 mA h g^{-1} and significantly surpassing that of NVPF, which is 91.1 mA h g^{-1} . The incorporation of rGO not only facilitates the formation of the nano-rectangular particles, but also enhances the electronic conductivity and increases the contact between the electrolyte and electrode, greatly optimizing the capacity. NVPF@rGO-3 has superior rate performance. As displayed in Fig. 3c, NVPF@rGO-3 exhibits reversible capacities of 148.7, 132.3, 110.4, 90.6, 75.5, and 59.6 mA h g^{-1} at different rates of 1, 2, 5, 10, 20, and 30C, respectively. Notably, the charging time at 30C is merely 40 seconds, rendering it suitable for fast-charging applications. Furthermore, the long-term cycling performance is obtained at 30C (4.29 A g^{-1}) in Fig. 3d, where NVPF@rGO-3 attains a supreme capacity of 64.4 mA h g^{-1} at 30C. Following 4000 cycles, the capacity is maintained at 41.9 mA h g^{-1} , exhibiting a capacity reduction of only 0.0098% per cycle. Conversely, the capacity of pure NVPF is just 20.1 mA h g^{-1} at the 1000th cycle. NVPF@rGO-3 features enhanced cycle characteristics and rate capacity in comparison to NVPF@rGO-1 and NVPF@rGO-2 (Fig. S6 and S7, ESI[†]), indicating that the appropriate nanoparticle size and carbon coating are beneficial for enhancing the performance. As shown in Fig. S8 (ESI[†]), NVPF has obvious advantages over other similar cathode materials.

To examine the fundamental causes of the enhanced electrochemical properties, multiple techniques were employed, including CVs at varying scan rates, galvanostatic intermittent titration technique (GITT), and electrochemical impedance spectroscopy (EIS) to assess the charge storage kinetics of the NVPF@rGO-3 electrode. The pseudocapacitive contribution of NVPF@rGO-3 significantly rises from 78.5 to 94.7%, while the contributions of NVPF range from 31.9 to 71.3% shown in Fig. S9 (ESI[†]). The high pseudocapacitance contributes to the superior rate performance for NVPF@rGO-3. GITT is used to ascertain the diffusion coefficient of Zn^{2+} ($D_{\text{Zn}^{2+}}$) throughout the charging and discharging operations. The $D_{\text{Zn}^{2+}}$ for NVPF@rGO-3 is about 10^{-8} – 10^{-10} $\text{cm}^2 \text{s}^{-1}$, suppressing the value for NVPF (10^{-9} – 10^{-12} $\text{cm}^2 \text{s}^{-1}$) shown in Fig. 4a and b. The heightened $D_{\text{Zn}^{2+}}$ is another factor contributing to the improved electrochemical properties. Besides, EIS curves displayed in Fig. 4c and Fig. S10 (ESI[†]), reveal that the charge transfer resistance (R_{ct}) values of NVPF@rGO-1 (256.1 Ω), NVPF@rGO-2 (221.6 Ω), and NVPF@rGO-3 (181.4 Ω) are all lower than pure NVPF (293.4 Ω), suggesting that the rGO network effectively enhances the electronic conductivity of the composite materials.

The Zn^{2+} storage mechanism of NVPF@rGO-3 is synergistically elucidated by *ex situ* XRD and *ex situ* XPS techniques. As shown in Fig. 4d, the diffraction peaks at 16.1° , 27.9° , and 32.6° move to higher angles, corresponding to the (101), (200), and



Fig. 3 (a) CV curves at 0.1 mV s^{-1} . (b) Cycling performance at 1C. (c) Rate performance. (d) Cycling performance at 30C.



Fig. 4 GITT curves at 1C and the calculated diffusion coefficient of (a) NVPF and (b) NVPF@rGO-3. (c) Nyquist plots of NVPF and NVPF@rGO-3. (d) *Ex situ* XRD of NVPF@rGO-3. (e) *Ex situ* XPS of NVPF@rGO-3.

(202) crystal planes during the charging process, respectively. This shift implies that the Na^+ extraction leads to a reduction of the interplanar distances. The insertion of Zn^{2+} drives the diffraction angles of the (101), (200), and (202) lattice planes to lower degrees during the discharging process. Simultaneously, in V 2p XPS spectrum (Fig. 4e), a noticeable transition is observed where the characteristic peaks migrate from an initial state of V^{3+} (517.4 eV for V 2p_{1/2} and 525.0 eV for V 2p_{3/2}) to V^{4+} (518.3 eV for V 2p_{1/2} and 525.8 eV for V 2p_{3/2}) upon charging to 1.8 V, and reverting back to V^{4+} after discharging to 0.6 V. In the fully discharged state, the obvious Zn^{2+} signal appears, indicating the incorporation of Zn^{2+} into the Na sites. A small Zn^{2+} signal is observed when charged to 1.8 V, due to the small amount of Zn^{2+} from the electrolyte adhering to the electrode surface. These observations imply a reversible Zn^{2+} insertion/extraction mechanism.

In this work, we have successfully prepared rGO-coated tetragonal NVPF through a hydrothermal method followed by a low temperature calcination. By optimizing the calcination temperature, the NVPF particles evolve into more uniform nano-rectangular blocks. The three-dimensional structure of rGO, in conjunction with the NVPF nano-rectangular particles offers a good conductive network with more active sites. Therefore, NVPF@rGO exhibits an efficient and stable zinc storage performance, achieving a capacity of 143.1 mA h g⁻¹ at 1C and a stable capacity of 41.9 mA h g⁻¹ after 4000 cycles at 30C. CVs, EIS, and GITT data demonstrate that the addition of rGO enhances pseudocapacitive behavior, increases $D_{\text{Zn}^{2+}}$, and reduces resistance, collectively contributing to the preminent zinc storage performance. Besides, the Zn^{2+} insertion/extraction mechanism is characterized by *ex situ* XPS and *ex situ* XRD. Therefore, NVPF@rGO is a promising polyanionic cathode for AZIBs.

This work was supported by the National Natural Science Foundation of China (no. 21905058).

Data availability

All data supporting this research are included in the main article and/or ESI.†

Conflicts of interest

There are no conflicts to declare.

Notes and references

- 1 S. Zhang, S. Li and Y. Lu, *eScience*, 2021, **1**, 163–177.
- 2 Y. Du, X. Wang, Y. Zhang, H. Zhang, J. Man, K. Liu and J. Sun, *Chem. Eng. J.*, 2022, **434**, 134642.
- 3 J. Guan, Q. Huang, L. Shao, X. Shi, D. Zhao, L. Wang and Z. Sun, *Small*, 2023, **19**, 2207148.
- 4 J. S. Ko, P. P. Paul, G. Wan, N. Seitzman, R. H. DeBlock, B. S. Dunn, M. F. Toney and J. Nelson Weker, *Chem. Mater.*, 2020, **32**, 3028–3035.
- 5 P. Yu, Y. Zeng, H. Zhang, M. Yu, Y. Tong and X. Lu, *Small*, 2019, **15**, 1804760.
- 6 N. Zhang, F. Cheng, Y. Liu, Q. Zhao, K. Lei, C. Chen, X. Liu and J. Chen, *J. Am. Chem. Soc.*, 2016, **138**, 12894–12901.
- 7 Y.-H. Du, X.-Y. Liu, X.-Y. Wang, J.-C. Sun, Q.-Q. Lu, J.-Z. Wang, A. Omar and D. Mikhailova, *Rare Met.*, 2022, **41**, 415–424.
- 8 W. Xiao, S. Yang, R. Jiang, Q. Huang, X. Shi, Y. H. Tsang, L. Shao and Z. Sun, *J. Mater. Chem. A*, 2024, **12**, 5530–5539.
- 9 S. Zheng, Q. Wang, Y. Hou, L. Li and Z. Tao, *J. Energy Chem.*, 2021, **63**, 87–112.
- 10 Y. Tian, Y. An, J. Feng and Y. Qian, *Mater. Today*, 2022, **52**, 225–249.
- 11 J. Hong, L. Xie, C. Shi, X. Lu, X. Shi, J. Cai, Y. Wu, L. Shao and Z. Sun, *Small Methods*, 2024, **8**, 2300205.
- 12 Y. Guo, L.-C. Xu, W. Zhao, C. Guo, Z. Yang, R. Liu, J.-L. Shao, L. Xue and X. Li, *Phys. Chem. Chem. Phys.*, 2022, **24**, 19362–19370.
- 13 M. Chen, S.-C. Zhang, Z.-G. Zou, S.-L. Zhong, W.-Q. Ling, J. Geng, F.-A. Liang, X.-X. Peng, Y. Gao and F.-G. Yu, *Rare Met.*, 2023, **42**, 2868–2905.
- 14 L. Linpo, L. Shuailei, L. Wencong, B. Deliang, W. Liu, G. Qiuyue, Y. Chen, H. Zuoqi, Y. Li and J. Liu, *Nano-Micro Lett.*, 2021, **13**, 1–14.
- 15 P. Hu, T. Zhu, X. Wang, X. Zhou, X. Wei, X. Yao, W. Luo, C. Shi, K. A. Owusu and L. Zhou, *Nano Energy*, 2019, **58**, 492–498.
- 16 W. Li, K. Wang, S. Cheng and K. Jiang, *Energy Storage Mater.*, 2018, **15**, 14–21.
- 17 Z. Wang, M. Zhou, L. Qin, M. Chen, Z. Chen, S. Guo, L. Wang, G. Fang and S. Liang, *eScience*, 2022, **2**, 209–218.
- 18 J. Zhao, J. He, X. Ding, J. Zhou, S. Wu and R. Huang, *J. Power Sources*, 2010, **195**, 6854–6859.
- 19 Z. Chuan-Xiang, H. Jian-Ping, Z. Gui-Wang and Z. Jian-Qing, *Chin. J. Inorg. Chem.*, 2007, **23**, 649–654.
- 20 J. Barker, M. Saidi and J. Swoyer, *Electrochem. Solid-State Lett.*, 2002, **6**, A1.
- 21 C. Chang, Y. Li, W. He, G. Li, W. Guo, P. Zhu, M. Yao and J. Feng, *Mater. Lett.*, 2017, **209**, 82–85.
- 22 D. Bin, Y. Wang, A. G. Tamirat, P. Zhu, B. Yang, J. Wang, J. Huang and Y. Xia, *ACS Sustainable Chem. Eng.*, 2021, **9**, 3223–3231.
- 23 M. Ling, Q. Jiang, T. Li, C. Wang, Z. Lv, H. Zhang, Q. Zheng and X. Li, *Adv. Energy Mater.*, 2021, **11**, 2100627.
- 24 T. Jin, Y. Liu, Y. Li, K. Cao, X. Wang and L. Jiao, *Adv. Energy Mater.*, 2017, **7**, 1700087.
- 25 W. Chang, X.-Y. Zhang, J. Qu, Z. Chen, Y.-J. Zhang, Y. Sui, X.-F. Ma and Z.-Z. Yu, *ACS Appl. Mater. Interfaces*, 2020, **12**, 41419–41428.
- 26 M. Ling, Z. Lv, F. Li, J. Zhao, H. Zhang, G. Hou, Q. Zheng and X. Li, *ACS Appl. Mater. Interfaces*, 2020, **12**, 30510–30519.
- 27 N. Zhang, M. Jia, Y. Dong, Y. Wang, J. Xu, Y. Liu, L. Jiao and F. Cheng, *Adv. Funct. Mater.*, 2019, **29**, 1807331.
- 28 J. Xu, E. Gu, Z. Zhang, Z. Xu, Y. Xu, Y. Du, X. Zhu and X. Zhou, *J. Colloid Interface Sci.*, 2020, **567**, 84–91.
- 29 M. J. Park, H. Y. Asl, S. Therese and A. Manthiram, *J. Mater. Chem. A*, 2019, **7**, 7159–7167.